Astron. Astrophys. 345, 925–935 (1999)

ASTRONOMY
AND
ASTROPHYSICS

# $H_2O$ from R Cas:
# ISO LWS-SWS observations and detailed modelling*

**Truong-Bach[1], R.J. Sylvester[2], M.J. Barlow[2], Nguyen-Q-Rieu[1], T. Lim[3], X.W. Liu[2], J.P. Baluteau[4], S. Deguchi[5], K. Justtanont[6], and A.G.G.M. Tielens[7]**

[1] Observatoire de Paris, DEMIRM and UMR 8540, 61 avenue de l'Observatoire, F-75014 Paris, France
[2] Department of Physics and Astronomy, University College London, Gower Street, London WC1E 6BT, UK
[3] The LWS Instrument-Dedicated Team, ISO Science Operations Center, P.O. Box 50727, E-28080 Madrid, Spain
[4] Laboratoire d'Astronomie Spatiale, CNRS, BP 8, F-13376 Marseille Cedex 12, France
[5] Nobeyama Radio Observatory, NAO, Minamimaki, Minamisaku, Nagano 384-13, Japan
[6] Stockholm Observatory, S-13336 Saltsjöbaden, Sweden
[7] Kapteyn Astronomical Institute, P.O. Box 800, 9700 AV Groningen, The Netherlands

Received 10 March 1998 / Accepted 12 March 1999

**Abstract.** We present 29–197 $\mu$m spectra of the oxygen-rich Mira variable star, R Cas, obtained with the Long- and Short-Wavelength Spectrometers (LWS and SWS) on board the Infrared Space Observatory (ISO). The LWS grating observations were made during two pulsational stellar phases, $\phi \sim 0.5$ and 0.2 in August 1996 and June 1997 when the stellar luminosity was near its minimum and mean values, respectively. The infrared flux at the latter epoch was $\sim$ 30–40% stronger than at the former. SWS grating observations were also made in June 1997. The spectrum presents a strong far-infrared (FIR) continuum and is rich in water lines suitable for use as circumstellar diagnostics.

We have constructed a circumstellar model which consistently treats radiative transfer, chemical exchanges, photodissociation, and heating and cooling effects. The overall FIR excitation field was scaled by a factor which varied with the stellar phase. By fitting the model to the observed FIR water line fluxes and continuum while adopting the stellar parameters based on the Hipparcos distance we have found a mass-loss rate of $\dot{M} \sim 3.4 \times 10^{-7} \mathrm{M}_{\odot}\,\mathrm{yr}^{-1}$ and a total *ortho* and *para* water vapour abundance (relative to $\mathrm{H}_2$) of $f \sim 1.1\times 10^{-5}$. The kinetic temperature and the relative abundances of $H_2O$, OH, and O in chemical equilibrium have been derived as functions of radial distance $r$. $H_2O$ excitation is mainly dominated by FIR emitted by dust grains. The deduced model continuum flux at 29–197 $\mu$m for the $\phi \sim$0.5 phase was 61% of the flux at $\phi \sim$0.2. Photodissociation by the FUV interstellar field and CO cooling effects operate farther out than the $H_2O$ excitation region. Our derived mass-loss rate of R Cas is similar to the value $6\times 10^{-7}$ $\mathrm{M}_{\odot}\,\mathrm{yr}^{-1}$ previously published for WHya, another oxygen-rich AGB star.

**Key words:** stars: individual: R Cas – stars: mass-loss – stars: abundances – stars: AGB and post-AGB – infrared: stars – molecular processes

## 1. Introduction

R Cas is a normal red giant, classified as an M star because its chemical composition is oxygen-rich, with an abundance ratio C/O $< 1$. It belongs to the Miras, a group of regularly pulsating cool stars. With a period of light variation larger than 1 year ($\sim$ 430 days), it is classified as a a long-period variable (LPV) star. It pulsates in the fundamental mode while most of LPV stars with periods shorter than 400 days pulsate in an overtone (van Leeuwen et al. 1997).

Mass loss is a fundamental process that drives the star's further evolution on the AGB branch and beyond. Mass loss by AGB stars also dominates the gas and dust injection budgets of the interstellar medium. The mechanism for exciting the Mira emission is not well understood. Bujarrabal et al. (1989) analysed CO ($J$=1-0) emission from R Cas observed with the IRAM 30m radiotelescope. This single low-excitation millimeter wavelength CO line can partially describe the outer part of the circumstellar envelope. Bujarrabal et al. (1989) estimated a stellar distance of 270 pc, i.e., about 2.5 times the recent Hipparcos measurement, and adopted the envelope characteristics of the carbon star IRC+10216 when deriving the physical parameters for R Cas. Thus, new analyses including observations of other molecules such as water vapour around R Cas are certainly of interest.

Because water vapour is abundant in the terrestrial atmosphere, stellar $H_2O$ spectra are often blended with telluric $H_2O$ emission/absorption rendering the astronomical lines unobservable, even with high-altitude airborne telescopes. Use of the Infrared Space Observatory (ISO) telescope can avoid this problem, which is inherent to ground-based observations. Infrared

---

*Send offprint requests to*: Truong-Bach (tbach@obspm.fr)

* Based on observations with ISO, an ESA project with instruments funded by ESA Members States (especially the PI countries: France, Germany, the Netherlands and the United Kingdom) and with the participation of ISAS and NASA.

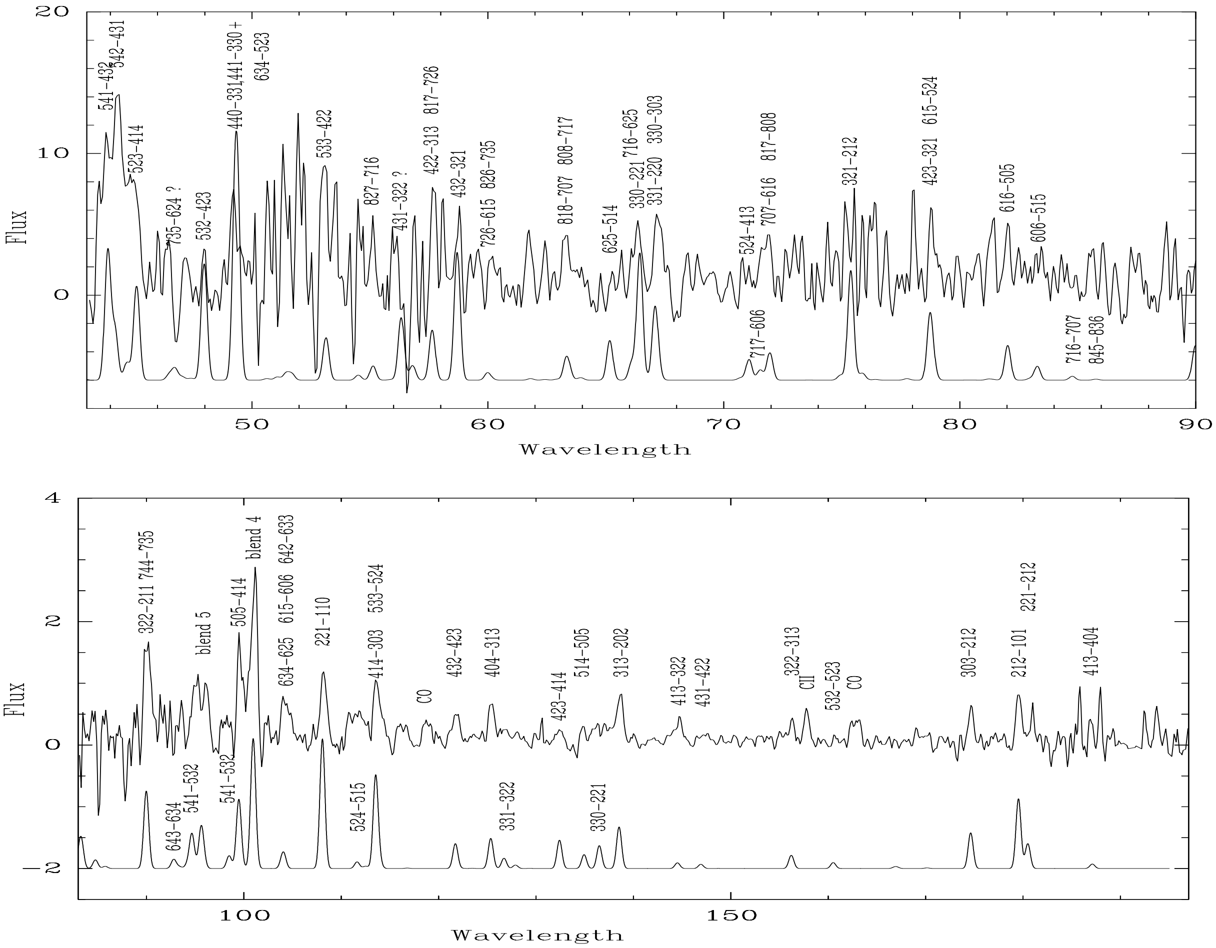

**Fig. 1.** LWS Observations I (see Table 1 for line fluxes): continuum-subtracted spectrum of R Cas. Our model spectrum is displayed offset for clarity. Units: $\mu$m and $10^{-15}$ W m$^{-2}$ $\mu$m$^{-1}$. For this and subsequent Figures, the model spectrum was produced by convolving the predicted total line fluxes with the appropriate spectral resolution element for the observations

(IR) radiation is emitted mainly from the innermost layers of the circumstellar environments. It is in this hot, high-density and strong radiation field region that atoms and molecules are highly excited. Thus, ISO observations would help us to understand the structure of the circumstellar envelope from the inner layers.

We present here the 29–197 $\mu$m ISO (LWS-SWS) spectrum of R Cas obtained in three sets of observations. Our circumstellar model used to fit the observed $H_2O$ line and continuum fluxes enabled us to derive some physical parameters of the stellar envelope: its mass loss rate, radial kinetic temperature, and radial molecular abundances.

## 2. Observations

Our first set of observations of R Cas, made on 5 August 1996 (hereafter Observations I) during Revolution 263 of the ISO mission, have been reported elsewhere (Truong-Bach et al. 1998, henceforth Paper I). This date corresponds to a stellar phase of 0.5, at minimum stellar luminosity. The spectrum is rather noisy. A second set of observations were obtained on 6 June 1997 (hereafter Observations II) during Revolution 568, using the same grating LWS01 AOT apparatus and procedure. This date corresponds to a stellar phase of 0.2, when the luminosity was decreasing to its mean value. The total on-target time was 2417 sec for Observations II. As for Observations I, the spectral resolution element is 0.3 $\mu$m in second order (SW1–SW5; $\lambda \leq$ 93 $\mu$m) and 0.6 $\mu$m in first order (LW1–LW5; $\lambda \geq 80$ $\mu$m) and the spectra were sampled at 1/4 of the resolution element. In order to form a complete spectrum from 43–197 $\mu$m, the sub-spectra from the ten LWS detectors were rescaled to give the same flux in regions of overlap. In almost all cases the fluxes were changed by less than 20%.

The merged LWS spectrum, which are continuum subtracted and labelled with some $H_2O$ transitions, are illustrated in Figs. 1–2. The $H_2O$ measured line fluxes for LWS are presented in Tables 1 and 2 with an estimated uncertainty $\sim$ 40% which increases toward shorter wavelengths. Note that the present Table 1 for Observations I revises and completes that given previously (see Paper I). The FIR emission from R Cas was about 40% stronger in Observations II than in Observations I.

A third set of observations were made during Revolution 564 (on 2 June 1997, hereafter Observations III), using the grating

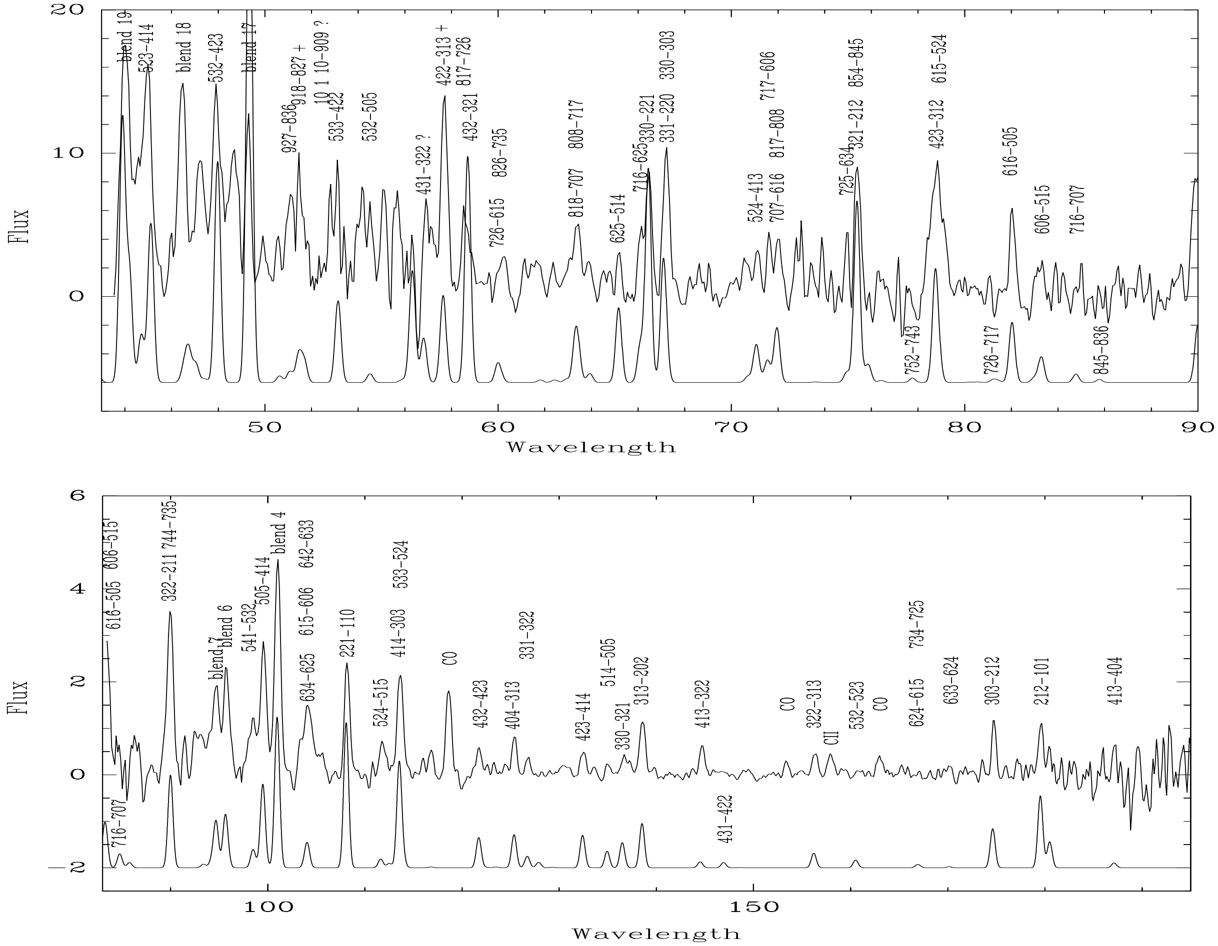

**Fig. 2.** LWS Observations II (see Table 2 for line fluxes): continuum–subtracted spectrum of R Cas. Our model spectrum is displayed offset for clarity. Units: $\mu$m and $10^{-15}$ W m$^{-2}$ $\mu$m$^{-1}$

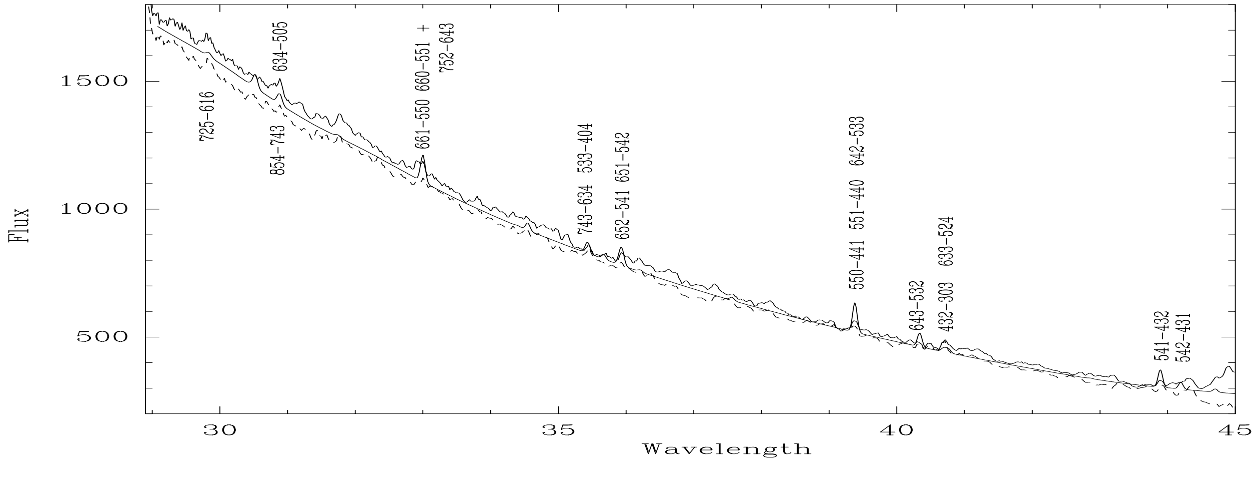

**Fig. 3.** SWS Observations III: observed forward (*solid*) and backward (*dashed*) spectra; an $H_2O$ model line spectrum is plotted with the average continuum for line identification. Units: $\mu$m and $10^{-15}$ W m$^{-2}$ $\mu$m$^{-1}$

SWS06 AOT. The total on-target time was 1718 sec. The SWS nominal resolution is $\sim 0.03\,\mu$m in the range 29–45 $\mu$m; however, because of rebinning in data-reduction, the model spectrum was convolved to a resolution lower ($\sim 0.08\,\mu$m) to reproduce the observed linewidths. To judge the SWS data quality, we plot in Fig. 3 the SWS forward and backward scans with their estimated average continuum superimposed with a set of model $H_2O$ lines for identification. Because of low s/n and blending, the averaged line fluxes (Table 3) can be uncertain by a factor of $\gtrsim 2$.

**Table 1.** Observations I: calculated ($F_{\rm cal1}$ and $F_{\rm cal1}$ for $r_{\rm min}$ =3.8× $10^{14}$ cm and 3× $10^{14}$ cm respectively, see text) and observed ($F_{\rm obs}$) $H_2O$ line fluxes, for R Cas

| $J$ | $K_-$ | $K_+$ | $J$ | $K_-$ | $K_+$ | $\lambda_{vac}$ ($\mu$m) | $\lambda_{obs}$ ($\mu$m) | Det. | $F_{\rm cal1}$ ( $10^{-15}$ W $m^{-2}$) | $F_{\rm cal2}$ | $F_{\rm obs}$ | Comments |
|---|---|---|---|---|---|---|---|---|---|---|---|---|
| 2 | 1 | 2 | 1 | 0 | 1 | 179.53 | 179.56 | LW4 | 0.77 | 0.81 | 0.60 | |
| 3 | 0 | 3 | 2 | 1 | 2 | 174.62 | 174.64 | LW4 | 0.40 | 0.43 | 0.45 | |
| 5 | 2 | 3 | 4 | 3 | 2 | 156.27 | 156.27 | LW4 | 0.02 | 0.03 | 0.18 | blend 1 |
| 3 | 2 | 2 | 3 | 1 | 3 | 156.19 | 156.27 | | 0.12 | 0.13 | | blend 1 |
| 4 | 1 | 3 | 3 | 2 | 2 | 144.52 | 144.60 | LW3 | 0.06 | 0.07 | 0.18 | noise |
| 3 | 1 | 3 | 2 | 0 | 2 | 138.53 | 138.59 | LW3 | 0.44 | 0.46 | 0.47 | |
| 5 | 1 | 4 | 5 | 0 | 5 | 134.93 | 134.82 | LW3 | 0.15 | 0.19 | 0.19 | |
| 4 | 2 | 3 | 4 | 1 | 4 | 132.41 | 132.60 | LW3 | 0.30 | 0.36 | 0.12 | noise |
| 3 | 3 | 1 | 3 | 2 | 2 | 126.71 | 126.94 | LW2 | 0.11 | 0.12 | 0.10 | noise |
| 4 | 0 | 4 | 3 | 1 | 3 | 125.35 | 125.36 | LW3 | 0.32 | 0.34 | 0.40 | |
| 4 | 3 | 2 | 4 | 2 | 3 | 121.72 | 121.76 | LW2 | 0.26 | 0.33 | 0.20 | |
| 5 | 3 | 3 | 5 | 2 | 4 | 113.95 | 113.74 | LW2 | 0.06 | 0.09 | 0.82 | blend 2 |
| 4 | 1 | 4 | 3 | 0 | 3 | 113.54 | | | 0.98 | 1.15 | | blend 2 |
| 7 | 4 | 3 | 7 | 3 | 4 | 112.51 | 112.17 | LW2 | 0.02 | 0.05 | 0.17 | |
| 5 | 2 | 4 | 5 | 1 | 5 | 111.63 | 111.22 | LW2 | 0.07 | 0.10 | 0.29 | |
| 2 | 2 | 1 | 1 | 1 | 0 | 108.07 | 108.20 | LW2 | 1.43 | 1.55 | 1.03 | |
| 6 | 3 | 4 | 6 | 2 | 5 | 104.09 | 103.96 | LW2 | 0.14 | 0.21 | 0.60 | blend 3 noise |
| 6 | 1 | 5 | 6 | 0 | 6 | 103.94 | | | 0.03 | 0.06 | | blend 3 |
| 6 | 4 | 2 | 6 | 3 | 3 | 103.92 | | | 0.02 | 0.04 | | blend 3 |
| 6 | 2 | 4 | 5 | 3 | 3 | 101.21 | 101.01 | LW1 | 0.02 | 0.03 | 1.96 | blend 4 |
| 2 | 2 | 0 | 1 | 1 | 1 | 100.98 | | | 1.02 | 1.08 | | blend 4 |
| 5 | 1 | 4 | 4 | 2 | 3 | 100.91 | | | 0.36 | 0.47 | | blend 4 |
| 5 | 0 | 5 | 4 | 1 | 4 | 99.49 | 99.65 | LW1 | 0.73 | 0.90 | 0.84 | |
| 4 | 4 | 0 | 4 | 3 | 1 | 95.88 | 95.42 | LW1 | 0.06 | 0.08 | 0.72 | blend 5 |
| 5 | 1 | 5 | 4 | 0 | 4 | 95.63 | | | 0.47 | 0.51 | | blend 5 |
| 7 | 4 | 4 | 7 | 3 | 5 | 90.05 | 90.08 | LW1 | 0.01 | 0.03 | 1.08 | blend 6 |
| 3 | 2 | 2 | 2 | 1 | 1 | 89.99 | | | 0.81 | 0.89 | | blend 6 |
| 6 | 1 | 5 | 5 | 2 | 4 | 78.93 | 78.83 | SW4 | 0.14 | 0.23 | 2.08 | blend 7 |
| 4 | 2 | 3 | 3 | 1 | 2 | 78.74 | | | 1.55 | 1.90 | | blend 7 |
| 3 | 2 | 1 | 2 | 1 | 2 | 75.38 | 75.40 | SW4 | 2.66 | 3.01 | 1.50 | |
| 7 | 0 | 7 | 6 | 1 | 6 | 71.95 | 71.78 | SW3 | 0.65 | 0.97 | 2.56 | blend 8 |
| 7 | 1 | 7 | 6 | 0 | 6 | 71.54 | | | 0.24 | 0.41 | | blend 8 |
| 5 | 2 | 4 | 4 | 1 | 3 | 71.07 | | | 0.48 | 0.65 | | blend 8 |
| 3 | 3 | 0 | 3 | 0 | 3 | 67.27 | 67.17 | SW3 | 0.09 | 0.11 | 1.87 | blend 9 |
| 3 | 3 | 1 | 2 | 2 | 0 | 67.09 | | | 1.70 | 1.90 | | blend 9 |
| 3 | 3 | 0 | 2 | 2 | 1 | 66.44 | 66.30 | SW3 | 2.95 | 3.55 | 1.74 | |
| 8 | 0 | 8 | 7 | 1 | 7 | 63.46 | 63.35 | SW3 | 0.14 | 0.31 | 1.61 | blend 10 |
| 8 | 1 | 8 | 7 | 0 | 7 | 63.32 | | | 0.48 | 0.86 | | blend 10 |
| 4 | 3 | 2 | 3 | 2 | 1 | 58.70 | 58.84 | SW2 | 2.97 | 3.69 | 1.25 | |
| 5 | 3 | 3 | 4 | 2 | 2 | 53.14 | 53.04 | SW2 | 0.99 | 1.34 | 2.51 | |
| 7 | 3 | 5 | 6 | 2 | 4 | 46.75 | 46.43 | SW1 | 0.25 | 0.51 | 2.55 | blend 11 noise+x? |
| 10 | 2 | 9 | 9 | 1 | 8 | 46.61 | | | 0.06 | 0.25 | | blend 11 |
| 6 | 3 | 3 | 6 | 0 | 6 | 46.54 | | | 0.01 | 0.03 | | blend 11 |
| 6 | 4 | 2 | 6 | 1 | 5 | 46.54 | | | 0.01 | 0.02 | | blend 11 |
| 3 | 3 | 1 | 2 | 0 | 2 | 46.48 | | | 0.09 | 0.10 | | blend 11 |
| 5 | 4 | 1 | 4 | 3 | 2 | 43.89 | 43.62 | SW1 | 3.03 | 4.20 | 3.84 | |

## 3. A model for $H_2O$ emission

Our previous modelling of $H_2O$ emission from W Hya (Barlow et al. 1996) (i) neglected excited vibrational states, (ii) did not use the observed FIR continuum as a constraint (iii) adopted the kinetic temperature distribution of Goldreich & Scoville (1976, hereafter GS) (iv) assumed a two-shell model of $H_2O$ abundances.

The present treatment abandons these assumptions. Here we add the first vibrational state to allow for 4–10 $\mu$m photon excitation. The $H_2O$ abundance starts from a guessed value at the inner radius with an initial ortho/para $H_2O$ ratio of 3. We solve

**Table 2.** Observations II: calculated ($F_{\rm cal1}$ and $F_{\rm cal2}$ for $r_{\rm min}$ =3.8× $10^{14}$ cm and 3× $10^{14}$ cm respectively, see text) and observed ($F_{\rm obs}$) $H_2O$ line fluxes for R Cas

| $J$ | $K_-$ | $K_+$ | $J$ | $K_-$ | $K_+$ | $\lambda_{vac}$ ($\mu$m) | $\lambda_{obs}$ ($\mu$m) | Det. | $F_{\rm cal1}$ | $F_{\rm cal2}$ | $F_{\rm obs}$ | Comments |
|---|---|---|---|---|---|---|---|---|---|---|---|---|
| | | | | | | | | | ($10^{-15}$ W $\rm m^{-2}$) | | | |
| 2 | 1 | 2 | 1 | 0 | 1 | 179.53 | 179.55 | LW5 | 0.97 | 1.01 | 0.82 | |
| 3 | 0 | 3 | 2 | 1 | 2 | 174.62 | 174.66 | LW4 | 0.52 | 0.55 | 0.54 | |
| 5 | 2 | 3 | 4 | 3 | 2 | 156.27 | 156.28 | LW4 | 0.04 | 0.04 | 0.24 | blend 1 |
| 3 | 2 | 2 | 3 | 1 | 3 | 156.19 | | | 0.17 | 0.17 | | blend 1 |
| 4 | 1 | 3 | 3 | 2 | 2 | 144.52 | 144.56 | LW4 | 0.08 | 0.09 | 0.29 | + CO 18–17 |
| 3 | 1 | 3 | 2 | 0 | 2 | 138.53 | 138.53 | LW3 | 0.61 | 0.61 | 0.74 | |
| 3 | 3 | 0 | 3 | 2 | 1 | 136.50 | 136.62 | LW3 | 0.34 | 0.38 | 0.18 | |
| 5 | 1 | 4 | 5 | 0 | 5 | 134.94 | 134.94 | LW3 | 0.23 | 0.28 | 0.18 | |
| 4 | 2 | 3 | 4 | 1 | 4 | 132.41 | 132.38 | LW3 | 0.44 | 0.50 | 0.35 | |
| 3 | 3 | 1 | 3 | 2 | 2 | 126.71 | 126.74 | LW3 | 0.16 | 0.17 | 0.14 | |
| 4 | 0 | 4 | 3 | 1 | 3 | 125.35 | 125.22 | LW3 | 0.45 | 0.48 | 0.41 | |
| 4 | 3 | 2 | 4 | 2 | 3 | 121.72 | 121.78 | LW2 | 0.41 | 0.48 | 0.31 | |
| 7 | 3 | 4 | 6 | 4 | 3 | 116.78 | 116.79 | LW2 | 0.01 | 0.02 | 0.36 | +x? |
| 5 | 3 | 3 | 5 | 2 | 4 | 113.95 | 113.62 | LW2 | 0.11 | 0.15 | 1.54 | blend 2 |
| 4 | 1 | 4 | 3 | 0 | 3 | 113.54 | | | 1.42 | 1.54 | | blend 2 |
| 5 | 2 | 4 | 5 | 1 | 5 | 111.63 | 111.76 | LW2 | 0.12 | 0.15 | 0.27 | |
| 2 | 2 | 1 | 1 | 1 | 0 | 108.07 | 108.04 | LW2 | 1.95 | 2.07 | 1.50 | |
| 6 | 3 | 4 | 6 | 2 | 5 | 104.09 | 104.23 | LW1 | 0.25 | 0.35 | 0.68 | blend 3 |
| 6 | 1 | 5 | 6 | 0 | 6 | 103.94 | | | 0.07 | 0.10 | | blend 3 |
| 6 | 4 | 2 | 6 | 3 | 3 | 103.92 | | | 0.04 | 0.07 | | blend 3 |
| 6 | 2 | 4 | 5 | 3 | 3 | 101.21 | 101.06 | LW1 | 0.04 | 0.05 | 2.57 | blend 4 |
| 2 | 2 | 0 | 1 | 1 | 1 | 100.98 | | | 1.50 | 1.51 | | blend 4 |
| 5 | 1 | 4 | 4 | 2 | 3 | 100.91 | | | 0.56 | 0.67 | | blend 4 |
| 8 | 2 | 6 | 8 | 1 | 7 | 99.98 | 99.57 | LW1 | 0.02 | 0.04 | 1.43 | blend 5 |
| 5 | 0 | 5 | 4 | 1 | 4 | 99.49 | | | 1.14 | 1.30 | | blend 5 |
| 5 | 4 | 1 | 5 | 3 | 2 | 98.49 | 98.49 | LW1 | 0.25 | 0.34 | 0.36 | |
| 4 | 4 | 0 | 4 | 3 | 1 | 95.88 | 95.73 | LW1 | 0.10 | 0.13 | 1.21 | blend 6 |
| 5 | 1 | 5 | 4 | 0 | 4 | 95.63 | | | 0.67 | 0.78 | | blend 6 |
| 4 | 4 | 1 | 4 | 3 | 2 | 94.71 | 94.70 | LW1 | 0.33 | 0.42 | 0.98 | blend 7 |
| 6 | 2 | 5 | 6 | 1 | 6 | 94.64 | | | 0.31 | 0.43 | | blend 7 |
| 7 | 4 | 4 | 7 | 3 | 5 | 90.05 | 89.81 | LW1 | 0.04 | 0.07 | 2.54 | blend 8 + x? |
| 3 | 2 | 2 | 2 | 1 | 1 | 89.99 | | | 1.24 | 1.31 | | blend 8 |
| 6 | 0 | 6 | 5 | 1 | 5 | 83.28 | 83.28 | SW5 | 0.57 | 0.75 | 0.78 | |
| 6 | 1 | 6 | 5 | 0 | 5 | 82.03 | 82.06 | SW4 | 1.34 | 1.64 | 1.36 | |
| 6 | 1 | 5 | 5 | 2 | 4 | 78.93 | 78.81 | SW5 | 0.27 | 0.40 | 2.94 | blend 9 |
| 4 | 2 | 3 | 3 | 1 | 2 | 78.74 | | | 2.42 | 2.74 | | blend 9 |
| 8 | 5 | 4 | 8 | 4 | 5 | 75.50 | 75.40 | SW4 | 0.06 | 0.14 | 3.0 | blend 10 |
| 3 | 2 | 1 | 2 | 1 | 2 | 75.38 | | | 3.92 | 4.24 | | blend 10 |
| 7 | 2 | 5 | 6 | 3 | 4 | 74.95 | 74.94 | SW4 | 0.24 | 0.38 | 0.64 | |
| 8 | 1 | 7 | 8 | 0 | 8 | 72.03 | 72.01 | SW3 | 0.03 | 0.07 | 1.36 | blend 11 |
| 7 | 0 | 7 | 6 | 1 | 6 | 71.95 | | | 1.20 | 1.61 | | blend 11 |
| 7 | 1 | 7 | 6 | 0 | 6 | 71.54 | 71.62 | SW3 | 0.50 | 0.76 | 1.18 | |
| 5 | 2 | 4 | 4 | 1 | 3 | 71.07 | 71.11 | SW3 | 0.85 | 1.07 | 1.01 | |
| 3 | 3 | 0 | 3 | 0 | 3 | 67.27 | 67.20 | SW3 | 0.13 | 0.14 | 3.16 | blend 12 |
| 3 | 3 | 1 | 2 | 2 | 0 | 67.09 | | | 2.72 | 2.94 | | blend 12 |
| 3 | 3 | 0 | 2 | 2 | 1 | 66.44 | 66.47 | SW3 | 4.68 | 5.20 | 3.07 | |
| 7 | 1 | 6 | 6 | 2 | 5 | 66.09 | 66.09 | SW3 | 0.83 | 1.24 | 1.08 | |
| 6 | 2 | 5 | 5 | 1 | 4 | 65.17 | 65.17 | SW3 | 1.67 | 2.21 | 0.61 | noisy |
| 8 | 0 | 8 | 7 | 1 | 7 | 63.46 | 63.31 | SW3 | 0.36 | 0.65 | 1.57 | blend 13 |
| 8 | 1 | 8 | 7 | 0 | 7 | 63.32 | | | 1.03 | 1.59 | | blend 13 |
| 8 | 2 | 6 | 7 | 3 | 5 | 60.16 | 60.16 | SW3 | 0.08 | 0.17 | 1.59 | blend 15 noise |
| 7 | 2 | 6 | 6 | 1 | 5 | 59.99 | | | 0.41 | 0.70 | | blend 15 |
| 4 | 3 | 2 | 3 | 2 | 1 | 58.70 | 58.58 | SW3 | 4.98 | 5.70 | 2.31 | |
| 8 | 1 | 7 | 7 | 2 | 6 | 57.71 | 57.70 | SW2 | 0.21 | 0.44 | 2.76 | blend 16 |
| 4 | 2 | 2 | 3 | 1 | 3 | 57.64 | | | 1.76 | 1.93 | | blend 16 |

**Table 2.** (Continued)

| $J$ | $K_-$ | $K_+$ | $J$ | $K_-$ | $K_+$ | $\lambda_{vac}$ ($\mu$m) | $\lambda_{obs}$ ($\mu$m) | Det. | $F_{\rm cal1}$ ($10^{-15}$ W m$^{-2}$) | $F_{\rm cal2}$ | $F_{\rm obs}$ | Comments |
|---|---|---|---|---|---|---|---|---|---|---|---|---|
| 4 | 3 | 1 | 3 | 2 | 2 | 56.33 | 56.81 | SW2 | 2.49 | 2.89 | | noisy |
| 8 | 2 | 7 | 7 | 1 | 6 | 55.13 | 55.10 | SW3 | 0.83 | 1.48 | 0.85 | noisy |
| 5 | 3 | 3 | 4 | 2 | 2 | 53.14 | 53.08 | SW3 | 1.82 | 2.30 | 1.32 | |
| 9 | 1 | 8 | 8 | 2 | 7 | 51.69 | 51.47 | | 0.47 | 1.04 | | noisy |
| 6 | 3 | 4 | 5 | 2 | 3 | 49.39 | 49.31 | SW1 | 3.07 | 4.12 | 4.10 | blend 17 noisy |
| 4 | 4 | 1 | 3 | 3 | 0 | 49.34 | | | 5.89 | 6.99 | | blend 17 |
| 4 | 4 | 0 | 3 | 3 | 1 | 49.28 | | | 3.03 | 3.74 | | blend 17 |
| 5 | 3 | 2 | 4 | 2 | 3 | 47.97 | 47.93 | SW1 | 4.92 | 6.09 | 3.28 | |
| 7 | 3 | 5 | 6 | 2 | 4 | 46.75 | 46.44 | SW1 | 0.62 | 1.08 | 5.60 | blend 18 noise/+x? |
| 10 | 2 | 9 | 9 | 1 | 8 | 46.61 | | | 0.27 | 0.75 | | blend 18 |
| 6 | 3 | 3 | 6 | 0 | 6 | 46.54 | | | 0.03 | 0.05 | | blend 18 |
| 6 | 4 | 2 | 6 | 1 | 5 | 46.54 | | | 0.03 | 0.05 | | blend 18 |
| 3 | 3 | 1 | 2 | 0 | 2 | 46.48 | | | 0.13 | 0.14 | | blend 18 |
| 5 | 2 | 3 | 4 | 1 | 4 | 45.11 | 45.00 | SW1 | 3.53 | 4.28 | 3.39 | |
| 5 | 4 | 2 | 4 | 3 | 1 | 44.20 | 43.98 | SW1 | 2.35 | 3.24 | 7.37 | blend 19 |
| 7 | 4 | 3 | 7 | 1 | 6 | 44.05 | | | 0.09 | 0.16 | | blend 19 |
| 5 | 4 | 1 | 4 | 3 | 2 | 43.89 | | | 5.75 | 7.30 | | blend 19 |

**Table 3.** Observations III: calculated ($F_{\rm cal1}$ and $F_{\rm cal2}$ for $r_{\rm min}$ =3.8× $10^{14}$ cm and 3× $10^{14}$ cm respectively, see text) and observed $H_2O$ line fluxes from R Cas

| $J$ | $K_-$ | $K_+$ | $J$ | $K_-$ | $K_+$ | $\lambda_{vac}$ ($\mu$m) | $\lambda_{obs}$ ($\mu$m) | Det. | $F_{\rm cal1}$ ( $10^{-15}$ W m$^{-2}$) | $F_{\rm cal2}$ | $F_{\rm obs}$ | Comments |
|---|---|---|---|---|---|---|---|---|---|---|---|---|
| 5 | 4 | 2 | 4 | 3 | 1 | 44.195 | 43.98 | SWS | 2.35 | 3.24 | 7.4 | blend 1 |
| 7 | 4 | 3 | 7 | 1 | 6 | 44.049 | | | 0.09 | 0.16 | | blend 1 |
| 5 | 4 | 1 | 4 | 3 | 2 | 43.893 | | | 5.75 | 7.30 | | blend 1 |
| 6 | 3 | 3 | 5 | 2 | 4 | 40.760 | 40.71 | SWS | 1.31 | 2.01 | 5.3 | blend 2 |
| 4 | 3 | 2 | 3 | 0 | 3 | 40.691 | | | 1.25 | 1.48 | | blend 2 |
| 6 | 4 | 2 | 5 | 3 | 3 | 39.399 | 39.38 | SWS | 1.90 | 2.94 | 3.9 | blend 3 |
| 5 | 5 | 1 | 4 | 4 | 0 | 39.380 | | | 2.46 | 3.71 | | blend 3 |
| 5 | 5 | 0 | 4 | 4 | 1 | 39.375 | | | 5.71 | 7.73 | | blend 3 |
| 7 | 4 | 4 | 6 | 3 | 3 | 37.566 | 37.55 | SWS | 0.98 | 1.82 | 2.2 | |
| 6 | 5 | 2 | 5 | 4 | 1 | 35.938 | 35.94 | SWS | 4.86 | 7.32 | 3.5 | blend 4 noise |
| 6 | 5 | 1 | 5 | 4 | 2 | 35.904 | | | 1.78 | 3.09 | | blend 4 |
| 5 | 3 | 3 | 4 | 0 | 4 | 35.472 | 35.45 | SWS | 0.49 | 0.65 | 2.5 | blend 5 |
| 7 | 4 | 3 | 6 | 3 | 4 | 35.428 | | | 3.45 | 5.61 | | blend 5 |
| 7 | 3 | 4 | 6 | 2 | 5 | 34.549 | 34.54 | SWS | 2.40 | 3.98 | 2.4 | |
| 6 | 6 | 1 | 5 | 5 | 0 | 33.005 | 33.01 | SWS | 4.13 | 6.96 | 5.6 | blend 6 |
| 6 | 6 | 0 | 5 | 5 | 1 | 33.005 | | | 1.50 | 2.91 | | blend 6 |
| 7 | 5 | 2 | 6 | 4 | 3 | 32.991 | | | 3.55 | 6.16 | | blend 6 |
| 4 | 4 | 1 | 3 | 1 | 2 | 31.772 | 31.77 | SWS | 0.13 | 0.17 | 5.1 | blend 7 |
| 8 | 4 | 4 | 7 | 3 | 5 | 31.738 | | | 0.60 | 1.33 | | blend 7 |
| 6 | 3 | 4 | 5 | 0 | 5 | 30.899 | 30.89 | SWS | 1.52 | 2.22 | 4.2 | blend 8 |
| 8 | 5 | 4 | 7 | 4 | 3 | 30.871 | | | 2.16 | 4.48 | | blend 8 |
| 5 | 4 | 2 | 4 | 1 | 3 | 29.885 | 29.85 | SWS | 0.10 | 0.15 | 5.0 | blend 9 |
| 7 | 2 | 5 | 6 | 1 | 6 | 29.837 | | | 1.20 | 1.97 | | blend 9 |

radiative transfer and thermal balance to derive a radial kinetic temperature $T_{\rm K}(r)$, $H_2O$ line fluxes, and the FIR continuum consistently in order to compare with the observations.

For R Cas, the Hipparcos parallax (van Leeuwen et al. 1997) corresponds to a distance of 107 ± 12 pc and $M_{\rm bol}$ = -3.74. Adopting the angular diameter E-model of Haniff et al. (1995) gives: the stellar radius $r_* \sim 2\times\,10^{13}$ cm, stellar effective temperature $T_{\rm eff} \sim$ 2415 K, stellar luminosity $L \sim$ 2420 $L_\odot$, and stellar mass $M \sim 1.2 M_\odot$. From CO observations, the outflow terminal velocity is $V_t$ = 12 $\rm km\,s^{-1}$ (Bujarrabal et al. 1989, Loup et al. 1993). We assumed an atomic-to-molecular hydrogen ratio of $f$ = 1. Collisional rates of *ortho*- and of *para*-$H_2O$

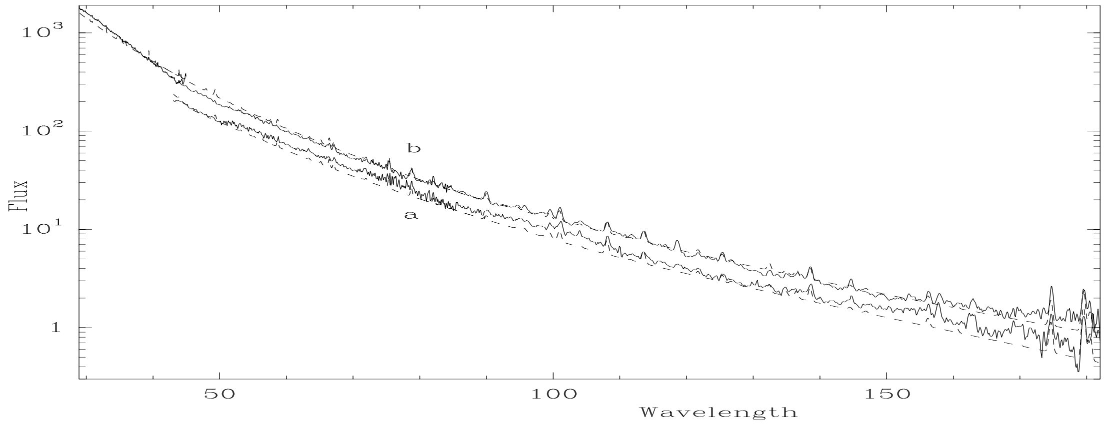

**Fig. 4.** Merged and smoothed FIR continuum spectra of: (a) Observations I; (b) Observation II-III. *Dotted*, model continuum spectra. Units: $\mu$ and $10^{-15}$ W m$^{-2}\mu$m$^{-1}$

**Table 4.** A 10-point sample of the observed FIR continuum fluxes used for the fit and their corresponding calculated values (in $10^{-15}$ W m$^{-2}\mu$m$^{-1}$)

| $\lambda$ ($\mu$) | 29 | 40 | 43 | 46 | 50 | 62 | 72 | 86 | 108 | 130 | 132 | 155 | 185 | 190 |
|---|---|---|---|---|---|---|---|---|---|---|---|---|---|---|
| Observations I | | | 200 | 165 | 125 | 65 | 37 | 16 | 5.7 | 2.6 | | 1.3 | 0.4 | |
| Calculated | | | 240 | 186 | 135 | 58 | 31 | 15 | 5.6 | 2.5 | | 1.1 | 0.4 | |
| Observations II-III | 1750 | 500 | | | 180 | 90 | 50 | 23 | 9 | | 3.5 | 1.75 | | 0.7 |
| Calculated | 1559 | 514 | | | 223 | 95 | 51 | 24 | 9.2 | | 4.0 | 1.85 | | 0.7 |

excited by He impact (Green et al. 1993) were corrected by a factor $\sim$ 1.38 to account for $H_2$ encounters. We treat 45 rotational levels of the ground vibrational state, $\nu_0$, whose highest energy is $\sim$ 2000 K. To account for $\sim$ 4–10 $\mu$ photon excitation, as suggested by Barlow et al. (1996), we considered also the 45 lowest rotational levels of the first excited vibrational state, $\nu_2$. We assumed that $\nu_2$ and $\nu_0$ have the same rotational collision rates, $C(JK_-K_+ - J'K'_-K'_+)$, while between $\nu_2$ and $\nu_0$ the vib-rotational collision rates are lower by a factor $\sim$ 0.01 (Deguchi & Nguyen-Q-Rieu 1990; hereafter D-NQR). This factor was subsequently varied by a factor of 10 to determine its effects. As in D-NQR, we found that uncertainties in the vibrational collisional rates have no effect on the calculated $H_2O$ line fluxes.

The FIR continuum radiation comes from the central star, the 2.7 K background, and dust. It was scaled by a factor, $W_s$, to account for the stellar phase dependence. The dust temperature varies as $r^{-0.4}$ (Elitzur et al. 1976). The FIR emissivity of dust grains was taken to vary as (80/$\lambda$($\mu$m))$^q$ (Bujarrabal et al. 1980), where we have found $q \sim$ 0.80 is appropriate to reproduce the observed wavelength dependence of the FIR continuum spectra (Fig. 4). We adopted a grain radius of $r_\mathrm{d}$=0.1 $\mu$m and a dust mass density $\varrho_\mathrm{d}$=3 g cm$^{-3}$. A dust–to–gas mass ratio of 0.005 seems to be appropriate (Groenewegen et al. 1998). If $n_\mathrm{d}$ is the grain number density, and $\sigma_\mathrm{d}$ is the grain geometrical cross section, uncertainties in the grain characteristics $n_\mathrm{d}\sigma_\mathrm{d}$ can be absorbed in the momentum transfer efficiency factor $Q$, a free parameter in the dust absorption coefficient, which is used to fit the observed $H_2O$ line fluxes and continuum:

$$k(\mathrm{cm}^{-1}) = Q n_\mathrm{d}\sigma_\mathrm{d} = -\frac{d\tau_\mathrm{d}}{dz}\ .$$

Here $\tau_\mathrm{d}(p, z)$ is the averaged optical depth of dust grains at 80 $\mu$m from -$\infty$ to $z$ along the line of sight at impact parameter $p$; $p$ and $z$ are the components of the radius vector $\mathbf{r}$ in the Castor (1970) coordinate system ($p$=0 and $z$=$r$ for the on-source direction).

In order to reduce the calculation time, we have fitted the model to a sample of 10 points of the observed FIR continuum spectrum (see Table 4). The entire continuum distribution can be obtained by interpolation, using a spline function (see Fig. 4).

Since the *ortho* states do not mix with the *para* states (Herzberg 1962, Townes & Schawlow 1975), we have distinguished two systems whose transition probabilities, collisional rates, and statistical weights [ 3(2$J$+1) for an *ortho* and 2$J$+1 for a *para* level $J$ ] are different. We assumed an initial ortho–to–para $H_2O$ abundance ratio of 3, which is expected to be equal to the high-temperature limit for $H_2O$ molecules newly formed on a grain surface (Tielens & Allamandola 1987). The gas velocity, $v_\mathrm{e}(r)$, was obtained by solving the equation of motion for the ejected gas (GS). The original expression for the drift velocity, $v_\mathrm{d}(r)$, of the moving grains relative to the gas particles is not valid close to the stellar atmosphere (GS). We used a modified expression for $v_\mathrm{d}(r)$ (Truong-Bach et al. 1991) based on the equation of motion of the grains (Kwok 1975). The molecular densities of $H_2O$, OH, and O were derived from the exothermic chemical equilibrium reactions

$$\mathrm{OH} + \mathrm{H_2} \leftrightarrows \mathrm{H_2O} + \mathrm{H} + 0.69\,\mathrm{eV}$$
$$\mathrm{OH} + \mathrm{H} \leftrightarrows \mathrm{O} + \mathrm{H_2} + 0.3\,\mathrm{eV}$$

Photodissociation by the interstellar UV field operates in the outer envelope according to

$$H_2O \xrightarrow{h\nu} OH \xrightarrow{h\nu} O$$

Here the unshielded photodissociation rates were taken to be (Roberge et al. 1991)

$$G(H_2O) = 5.9\,10^{-10}\,s^{-1}$$
$$G(OH) = 3.5\,10^{-10}\,s^{-1}$$

$H_2O$ self-shielding is negligible. Dust shielding against the UV interstellar field is represented by a dust opacity at 1000 Å (Morris & Jura 1983). Because the local line width due to turbulence and thermal broadening ($\sim$ 0.3–0.7 $\mathrm{km\,s^{-1}}$) is much lower than the terminal velocity (12 $\mathrm{km\,s^{-1}}$), one can expect that photons which escape from a local volume are not reabsorbed, and use the escape probability formalism (Castor 1970) to perform the statistical equilibrium calculations. The deduced level populations were used to determine molecular line opacities, excitation temperatures, and fluxes. We have included heating and cooling and photodissociation by FUV interstellar field (e.g. Truong-Bach et al. 1990, 1991) together with chemical reactions (GS) in our calculations.

Heating of gas is due to collisions with dust grains and also by exothermic (chemical and photodissociating) reactions. Cooling is due to: (i) the gas adiabatic expansion (GS); (ii) $H_2O$ spontaneous emission between rotational levels (of $\nu_0$ and $\nu_2$) whose fractional level populations are determined by solving the statistical equilibrium equations (see Truong-Bach et al. 1990); (iii) $H_2$ decay from the first excited to the ground vibrational state (GS). We also estimated cooling by CO emission in a three-level scheme: two rotational levels in the ground vibrational state and one in the excited vibrational state (e.g. GS; Justtanont et al. 1994). With a CO/$H_2$ abundance of 4× $10^{-4}$ at the inner radius (Mamon et al. 1988), we found that CO cooling operates farther out than the $H_2O$ excitation region. $H_2O$ molecules formed in the vibrationally-excited state (and the reverse, dissociation, reaction) were found to have a negligible effect on the energy balance of the envelope, in agreement with the results of Justtanont et al. (1994).

The net energy variation is related to the temperature gradient throughout the shell. Thus, when the best fit to the observations was achieved, the molecular abundances and densities, the heating and cooling rates, and the kinetic temperature, $T_K(r)$, were simultaneously derived.

## 4. Results and discussion

In Figs. 1 and 2 we plot the $H_2O$ model spectra superimposed on the observed spectra of observations I and II for comparison. The fit for the long-wavelength portion (i.e. detectors LW1–5) of the LWS spectrum (lower panel of Figs. 1 and 2) seems to be better than for the short-wavelength detectors (upper panels). This is, to a large extent, due to the high continuum/line flux ratio toward short wavelengths, causing the difficulty in determining the baseline among the continuum fluctuations. Fig. 4 represents the spectra with continuum: the rapid rise of the continuum toward 29 $\mu$m, the low line/continuum ratios, and blending are the main causes of uncertainty. At some wavelength positions, the forward and backward scans of SWS (Fig. 3, see Sect. 2) do not clearly show the same lines when the continuum fluctuations can be comparable to the line heights. Uncertainties in line fluxes, determined after continuum removal, are estimated to be better than $\sim$ 40% for LW. They increase toward SW and can reach a factor 2–3 for SWS. The measured line fluxes are listed in Tables 1–3 (see Sect. 2).

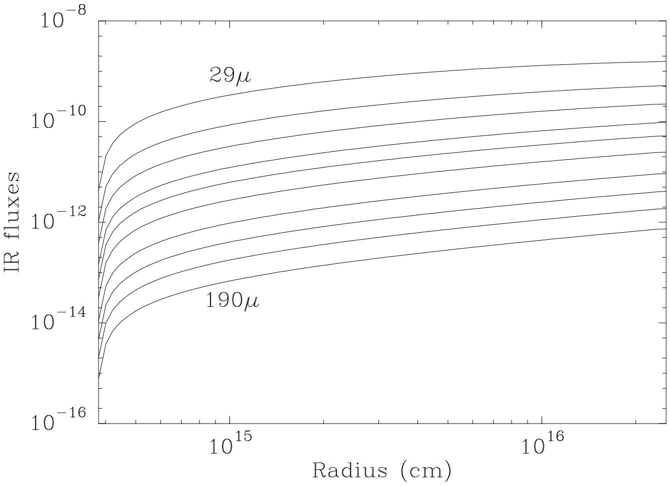

**Fig. 5.** The FIR fluxes (in W $m^{-2}\mu m^{-1}$) at 29, 40, 50, 62, 72, 86, 108, 130, 155 and 190 $\mu$m as functions of radius (*from top to bottom, respectively)*

Our best fit to the observed FIR continuum and $H_2O$ line fluxes (Observations I-III) was obtained with a mass loss rate of $\dot{M} \sim$ 3.4× $10^{-7}$ $M_\odot\,yr^{-1}$, and a $H_2O$ total initial relative abundance of $\sim$1.1×$10^{-5}$ (7.9×$10^{-6}$ for *ortho*- and 2.7×$10^{-6}$ for *para*- $H_2O$). The scaling factor for FIR excitation, $W_s$ (Sect. 3), was found to be $\sim$ 0.61 and 1 for Observations I and II-III, respectively. SW and SWS lines are excited closer to the star ($r \lesssim$ 1.4× $10^{15}$ cm for line $\lambda 45.11\,\mu$m) than LW's ($r \lesssim$ 6.3× $10^{15}$ cm for line $\lambda 174.62\,\mu$m). Increasing the mass loss rate by 20% would lead to an increase of the line fluxes of $\sim$ 25% and 40% for the 174.62 $\mu$m and 45.11 $\mu$m lines, respectively. In an outward integration over a large range of radius, from $r$ = 1.0× $10^{14}$ cm to 2.5× $10^{16}$ cm, we determined the contributions to the line and continuum fluxes at each step. This allowed us to estimate an overall best fit for $r_{\min}$ =3.8× $10^{14}$ cm. A smaller value of $r_{\min}$ would overestimate the SWS+SW line fluxes, as reported in Tables 1 and 2. Here $H_2O$ line fluxes, $F_{\mathrm{calc1}}$ and $F_{\mathrm{calc2}}$, were calculated for 2 values of $r_{\min}$: $\sim$ 3.8× $10^{14}$ cm and 3.0× $10^{14}$ cm, respectively. In the following we adopt $r_{\min}$ = 3.8× $10^{14}$ cm. We note that most of the $H_2O$ line excitation arises at radii $\lesssim$ 5× $10^{15}$ cm. Within observational uncertainty, an outer radius $r_{\max}$ chosen greater than 1× $10^{16}$ cm makes little difference to the line fluxes. The outer shell from $r$= 1× $10^{16}$ cm to 2.5× $10^{16}$ cm contributes $\sim$ 16% to the FIR continuum at 29 $\mu$m, *i.e.*, within the observation uncertainty. The calculated intensities for $H_2O$ vibrationally-excited lines of $\nu_2$ were found

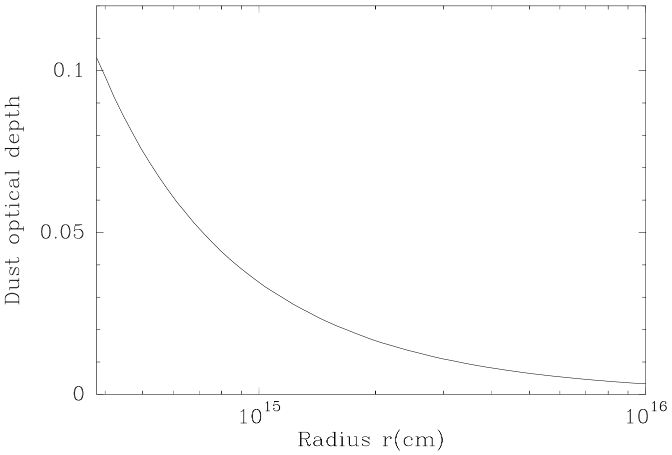

**Fig. 6.** The averaged optical depth of dust grains at 80 $\mu$m from $r$ to $\infty$

to be weak compared to those in the ground vibrational state, in agreement with the D-NQR model. In order to see the influence of collisional excitation from the ground to the vibrational levels, we multiplied the assumed vibrational collisional rates by a factor of 10. However the calculated $H_2O$ line fluxes in the fundamental state are not appreciably increased. On the other hand, when we decreased the FIR radiation field by a factor of 0.5, we have found that the $H_2O$ line fluxes decrease by e.g., 35% and 46% for the $\lambda$ 174.62 $\mu$m and 99.49 $\mu$m lines. If we take out the vibrational levels, the line fluxes would decrease by $\sim$ 61% and 57% for $\lambda$ 174.62 $\mu$m and 45.11 $\mu$m, respectively. From this new level configuration, if we vary the collisional rates by a factor of 2 these line fluxes would increase by $\sim$ 6%. These tests indicate that FIR radiative effects are more important than collisions in the excitation of $H_2O$. This finding opposes that of D-NQR and Barlow et al. (1996) which found that the FIR $H_2O$ lines are mainly excited by collisions. However it is not easy to compare these models with the present because they are fundamentally different and they did not constrain FIR continuum fluxes.

Fig. 6 gives the averaged optical depth of dust grains at 80 $\mu$m in the outflow. It decreases from $\sim$ 0.1 to $\sim$ 0.035 as $r$ increases from $r_{\rm min}$ to $\sim 1\ 10^{15}$ cm.

In Fig. 7, we plot the expansion velocity, $v_{\rm e}(r)$, of the circumstellar gas, the drift velocity, $v_{\rm d}(r)$, of dust grains relative to the gas, and the logarithmic velocity gradient, $\epsilon(r) = dlnv_e/dlnr$, as functions of radius $r$. Here we have set $\epsilon = 0.02$ for $\epsilon$ lower than this value as discussed by D-NQR for the large velocity gradient approximation, but numerical tests show that the modelling results are insensitive to the adopted limiting value of $\epsilon$.

The $H_2O$ line fluxes were calculated neglecting any possible non-local self-absorption effect (Nguyen-Q-Rieu et al. 1984, Morris et al. 1985). This is a good approximation since the change to the (optically thin/thick) line profile due to that effect is small, as it would enhance the redshifted wing while depressing the blueshifted one (Morris et al. 1985, Truong-Bach et al. 1991). Another characteristic of the self-absorbed line is the appearance of a weak shelf on the blue wing when self-absorption does not reduce the intensity entirely to zero. The width of this shelf increases with the line opacity (Morris et al. 1985). The low spectral resolutions of our observations do not allow us to discern the line profiles. It would be of interest to make higher-resolution observations of the IR line profiles. The optical depths at line centre (radial velocity $v_{//} = 0$, Castor 1970) and along the line of sight at projected distance in the plane of the sky $p \sim 1\times 10^{15}$ cm are $\sim$ 3.56, 1.40, and 0.15 for the 174.62 $\mu$m, 99.49 $\mu$m (505–411), and 45.11 $\mu$m lines, respectively.

In Fig. 8, we plot the heating and cooling rates. The momentum transfer efficiency used is $Q \sim 0.073$. We recall that $Q$ is linked to the grain characteristic factor $n_{\rm d}\sigma_{\rm d}$ in the dust absorption coefficient. A lower (or higher) value of $Q$ means a higher (or lower) value of $n_{\rm d}\sigma_{\rm d}$ for the fit. Grain-gas collisions dominate the heating effects. Cooling by gas adiabatic expansion is important throughout the envelope. Cooling by $H_2$ $v$ =1-0 pho-

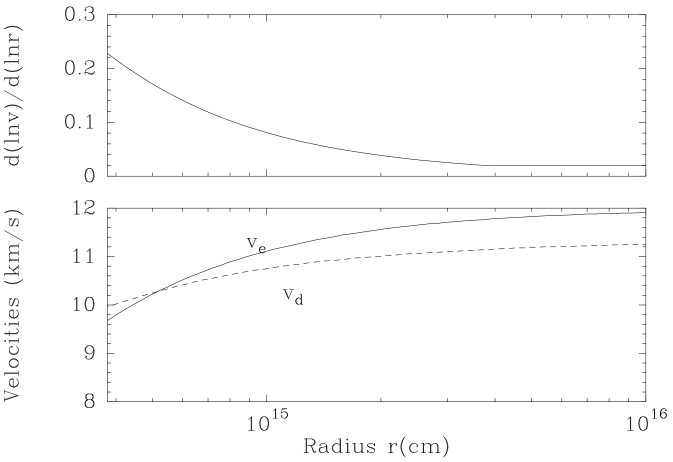

**Fig. 7.** (*Top*): the logarithmic velocity derivative $\epsilon(r)$ (in cgs units). (*Bottom*): the gas expansion velocity $v_{\rm e}$ and the drift velocity of dust grains $v_{\rm d}$ as functions of $r$

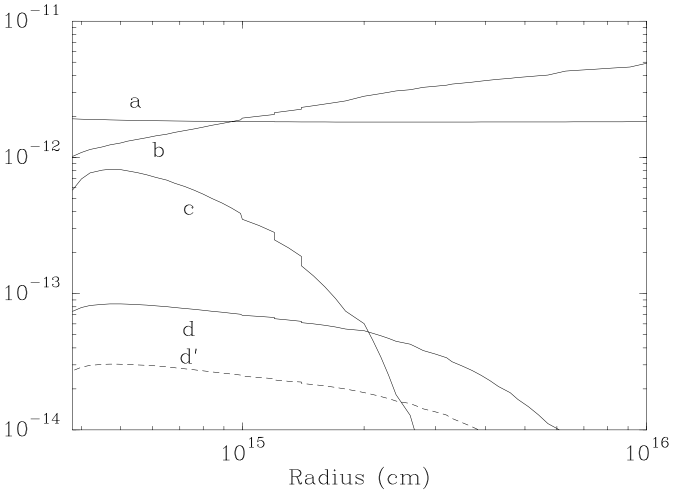

**Fig. 8.** The heating and cooling rates scaled by $(r/10^{14}\,{\rm cm})^4$ (in erg cm$^{-3}$ s$^{-1}$). *a*, grain-gas heating. Cooling due to: *b*, adiabatic expansion of gas; *c*, $H_2$ vibrational excitation; *d*, $H_2O$ rotational excitation. *Solid*, ortho; *dashed*, para $H_2O$

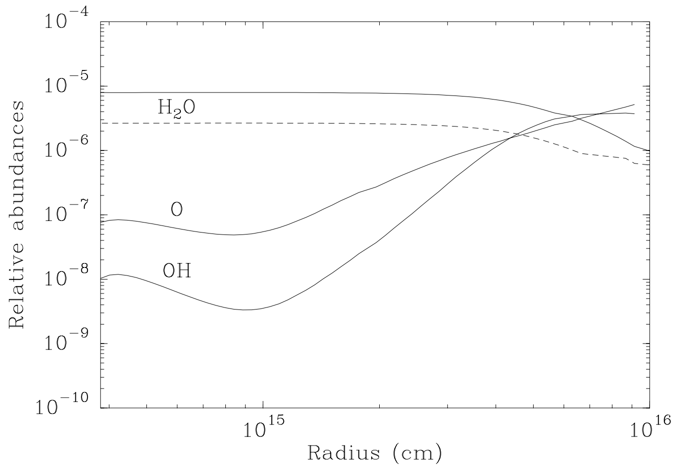

**Fig. 9.** The radial abundances of $H_2O$, O, and OH as functions of $r$ for Observations II. *Solid*, ortho; *dotted*, para $H_2O$

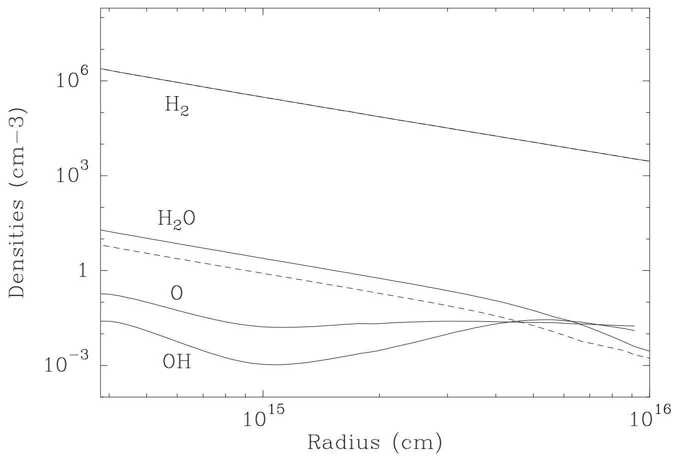

**Fig. 10.** The radial density distributions of $H_2$ and $H_2O$, O, and OH for Observations II. *Solid*, ortho; *dotted*, para $H_2O$

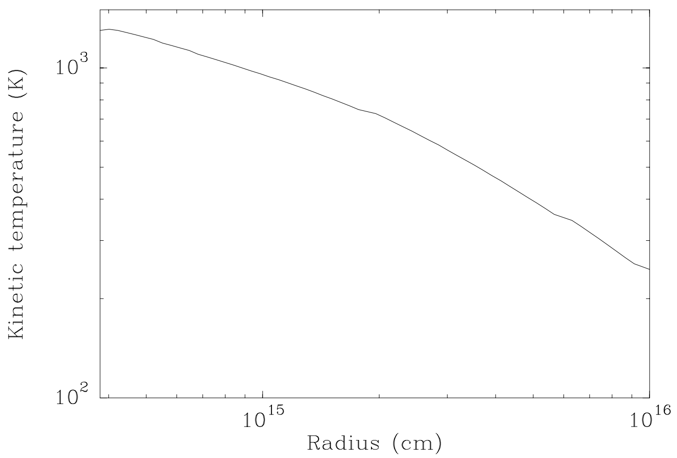

**Fig. 11.** The radial kinetic temperature distribution $T_{\rm K}(r)$

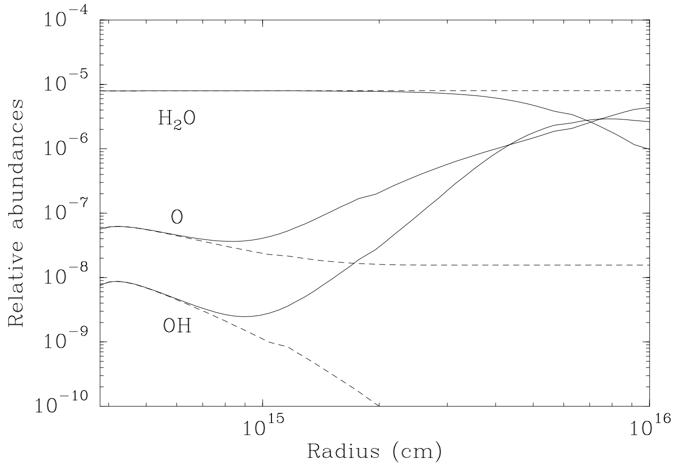

**Fig. 12.** The radial abundances of $H_2O$ (*ortho*), O, and OH. *Solid*, with UV photodissociation; *dotted*, without photodissociation

tons is important close to the central star. CO cooling is weak and operates outside of the $H_2O$ excitation region.

Fig. 9 shows the radial abundances of $H_2O$ in chemical equilibrium with O and OH. The *ortho*–to–*para* abundance ratio which starts from the value $\sim 3$ in the centre remains unchanged through the entire shell. Fig. 10 represents the densities of $H_2$, $H_2O$, OH, and O.

Fig. 11 shows the kinetic temperature distribution, $T_{\rm K}(r)$, in the envelope. It decreases outward from $\sim$ 1300 K. At radius $r \sim 10^{15}$ cm, the kinetic temperature is still $\sim$ 950 K. At $r \sim 5\times 10^{15}$ cm, it becomes $\sim$ 380 K. From here the excitation becomes too low to contribute significantly to the observed line fluxes.

In Fig. 12 we plot the radial abundances of $H_2O$ (*ortho*), O, and OH for two cases: with and without photodissociation. The weak dust shielding would allow interstellar FUV to penetrate deeply into the inner shell, since photoproduction of O and OH begins at $r \sim 7\times 10^{14}$ cm. However their abundance variations are weak compared to the $H_2O$ abundance itself. The figure shows that the $H_2O$ abundance is perceptibly decreased by photodissociation from $r \gtrsim 2.2\times 10^{15}$ cm. Here $H_2O$ excitation becomes low and the outer layers contribute typically $\sim$ 14–20% to LW ($\lambda$ 174.62 $\mu$m and 108.07 $\mu$m), but insignificantly to SWS ($\lambda$ 45.11 $\mu$m and 29.87$\mu$m) line fluxes.

Uncertainty of the derived mass loss and $H_2O$ abundance due to uncertain thermodynamics can be estimated. We recall that the kinetic temperature depends on the drift velocity which varies as $(Qv_e)^{0.5}$. If we varied this quantity, for example by decreasing $Q$ by $\delta Q$ = 50% $Q$, the calculated line fluxes would noticeably decrease by, e.g., 80%, 92%, and 98% for the LW 174.62 $\mu$m, SW 82.03 $\mu$m, and SWS 34.549 $\mu$m lines, respectively. For a moderate decrease of $Q$, $\delta Q$ = 30%$Q$, the latter line intensities would decrease only by 30%, 31%, and 50%, respectively, i.e., by about their observed uncertainties. We tried to compensate this line flux diminution by increasing the mass-loss rate by $\delta \dot{M}$ = 25% $\dot{M}$, and the intensity deviations were reduced to 0.6%, 8%, and 19%, respectively. This means that the new fit obtained is still good for LW but worse for shorter wavelengths. Therefore the upper limit of uncertainty for the mass loss can be estimated as 25%. Accordingly, the uncertainties for the $H_2O$ abundance and the kinetic temperature at the inner radius were derived to be 47% and 33%, respectively. Naturally the final uncertainty should include that from the Hipparcos distance determination (van Leuuwen et al. 1997).

## 5. Conclusion

Within the uncertainties encountered in the observations as discussed, Figs. 1, 2 & 4 and Tables 1–3 show acceptable comparisons between the predicted and observed integrated $H_2O$ spectra and FIR continua. The error bars for observed SWS line fluxes are nevertheless high by a factor 2–3; and it is interesting to perform new observations in this wavelength region. Some CO and CII lines are also found in the $H_2O$ spectra but their investigation is outside the scope of this paper. Observations I show a spectrum about $\sim$ 30–40% less intense compared to Observations II's where new or stronger lines appear and some components of a blend become clearly visible. This light variation due to stellar pulsations of the Mira variable between $\sim$ 300 days corresponds to a phase variation from 0.5, at minimum luminosity, to 0.2 where the luminosity was falling down to its mean value. A best fit to the overall spectra were obtained with the dilution factor for the FIR field scaled by a factor $\sim$ 0.61 and 1, respectively. This FIR field is mainly dominated by dust. Photodissociation of $H_2O$ by the interstellar UV field does not affect significantly the FIR $H_2O$ line fluxes, since the effect operates in the outer region ($\gtrsim 10^{16}$ cm) where $H_2O$ excitation temperatures become weak. The derived $H_2O$ abundance and density, the FIR continuum, and the kinetic temperature vary as functions of radius across the circumstellar envelope of R Cas. The derived mass-loss rate is $\dot{M} \sim 3.4\times 10^{-7}$ $\mathrm{M_\odot\ yr^{-1}}$. The deduced total (ortho and para) $H_2O$ abundance is $\sim 1.1\times 10^{-5}$ and the kinetic temperature is $T_k \sim 1300$ K at the inner radius of the envelope, and they decrease with distance from the star. Compared to W Hya, another O-rich AGB star, the initial $H_2O$ abundance of R Cas is about one order of magnitude lower while the mass-loss rate is nearly the same; the values found for W Hya ($1.2\times 10^{-4}$ and $6\times 10^{-7}$ $\mathrm{M_\odot\ yr^{-1}}$; see Barlow et al. 1996) were determined, however, by using a different model. Similar mass-loss rates ( $10^{-7}$ $\mathrm{M_\odot\,yr^{-1}}$) have been derived for a number of LPV Miras using CO radio observations (e.g. Knapp et al. 1982, Loup et al. 1993, Kahane & Jura 1994, Gonzalez-Alfonso et al. 1998), and optical KI/NaI scattering (e.g. Guilain & Mauron 1996).

*Acknowledgements.* It is a pleasure to thank F. Viallefond for supplying one of us (T.B.) with the GIPSY software for data reduction.

## References

Barlow M.J., Nguyen-Q-Rieu, Truong-Bach, et al., 1996, A&A 315, L241
Bujarrabal V., Guibert J., Nguyen-Q-Rieu, Omont A., 1980, A&A 311
Bujarrabal V., Gomez-Gonzalez J., Planesas P., 1989, A&A 219, 256
Castor J.I., 1970, MNRAS 149, 111
Deguchi S., Nguyen-Q-Rieu, 1990, ApJ 360, L27 (*cited as* D-NQR)
Elitzur M., Goldreich P., Scoville N., 1976, ApJ 205, 384
Goldreich P., Scoville N., 1976, ApJ 205, 144 (*cited as* GS)
Gonzalez-Alfonso, Cernicharo J., Alcolea J., et al., 1998, A&A 334, 1016
Green S., Maluendes S., McLean A.D., 1993, ApJS 85, 181
Groenewegen M.A.T., van der Veen W.E.C.J., Matthews H.E., 1998, A&A (in press)
Guilain C., Mauron M., 1996, A&A 314, 585
Haniff C.A., Scholz M., Tuthill P.G., 1995, MNRAS 276, 640
Herzberg G., 1962, Infrared and Raman spectra. D. Van Nostrand, London, p. 53
Justtanont K., Skinner C.J., Tielens A.G.G.M., 1994, ApJ 435, 852
Kahane C., Jura M., 1994, A&A 290, 183
Knapp G.R., Phillips T.G., Leighton B.R., et al., 1982, ApJ 252, 616
Kwok S., 1975, ApJ 198, 583
Loup C., Forveille T., Omont A., Paul J.F., 1993, A&AS 99, 291
Mamon G., Glassgold A.E., Huggins P.J., 1988, ApJ 328, 797
Morris M., Jura M., 1983, ApJ 264, 546
Morris M., Lucas R., Omont A., 1985, A&A 142, 107
Nguyen-Q-Rieu, Bujarrabal V., Olofsson H., Johansson L.E.B., Turner B.E., 1984, ApJ 286, 276
Roberge W.G., Jones D., Dalgarno A., 1991, ApJ 77, 287
Tielens A.G.G.M., Allamandola L.J., 1987, In: Hollenbach D.J., Thronson H.A. Interstellar Processes. Vol. 134, Reidel, Dordrecht, Holland, p. 397
Townes C.H., Schawlow A.L., 1975, Microwave spectroscopy. Dover, New York, p. 104
Truong-Bach, Morris D., Nguyen-Q-Rieu, Deguchi S., 1990, A&A 230, 431
Truong-Bach, Morris D., Nguyen-Q-Rieu, 1991, A&A 249, 435
Truong-Bach, Nguyen-Q-Rieu, Sylvester R.J, et al., 1998, Ap&SS 255, 325 (*cited as* Paper I)
van Leeuwen F., Feast M.W., Whitelock P.A., Yudin B., 1997, MNRAS 287, 955